

---

A NUMERICAL INVESTIGATION OF THE ENERGY  
TRANSFER OF A BODY UNDER FLUIDELASTIC  
GALLOPING

---

BY H.G.K.G JAYATUNGA

A THESIS SUBMITTED TO MONASH UNIVERSITY IN FULFILMENT OF THE REQUIREMENTS  
FOR THE DEGREE OF

DOCTOR OF PHILOSOPHY

Department of Mechanical Engineering

Monash University

October 2015



# CONTENTS

---

<b>1</b>	<b>Introduction</b>	<b>2</b>
1.0.1	Static body results . . . . .	4
1.0.2	Formulation of the new dimensionless groups $\Pi_1$ and $\Pi_2$ . . . . .	5
1.0.3	Comparison of $\Pi_1$ and $\Pi_2$ with classical VIV parameters . . . . .	8
1.0.4	Comparison of power between high and low $Re$ data . . . . .	8
1.0.5	Dependence on mass-stiffness, $\Pi_1$ . . . . .	10
1.0.6	Dependence on the mass ratio $m^*$ . . . . .	14

# CHAPTER 1

---

## INTRODUCTION

The review of published literature reveals that fluid-elastic galloping has a potential to be used as a mechanism for energy extraction (Barrero-Gil et al., 2010). Thus, the following questions emerged. What are the optimum parameters for energy transfer in a galloping system? How do they influence galloping?

Another fluid-structure interaction phenomenon, vortex-induced vibration (VIV), has also been investigated as a candidate for the power extraction from flows. The work from Bernitsas et al. (2008, 2009); Raghavan and Bernitsas (2011); Lee and Bernitsas (2011) and others from the same group at the University of Michigan have made significant progress with this problem. Therefore it may seem, at least initially, reasonable to present data from the fluid-elastic problem in the same parameters as typically used in VIV studies, which could be observed in current literature on galloping (Barrero-Gil et al., 2009, 2010; Parkinson and Smith, 1964).

However, the data presented in the pioneering study on energy harvesting from galloping (Barrero-Gil et al., 2010) presented using classical VIV parameters (i.e.  $U^*$ ,  $m^*\zeta$ ), shows that the mean power data does not collapse well. The reason behind this would be the difference in time-scales of VIV and galloping. Thus the work presented in this chapter is focused on testing this hypothesis and obtain the optimum conditions for mean power output.

Since the the Quasi-steady state model is the primary mathematical model used to model galloping in this study, the fluid-dynamic characteristics of flow over a static body

---

are presented and discussed first as it is the . Then, the natural time scales of the system are obtained using the linearised QSS model. Next, the new non-dimensional governing parameters  $\Pi_1$  and  $\Pi_2$ , are formulated by non-dimensionalising the QSS model from these natural time scales, followed by a comparison of galloping data using the classical VIV parameters and  $\Pi_1$  and  $\Pi_2$ . Then, the influence of  $\Pi_1$  and  $\Pi_2$  and the conditions for an optimum power output are discussed from QSS data. Finally, the QSS data are compared and discussed against FSI direct numerical simulations and final conclusions are presented.

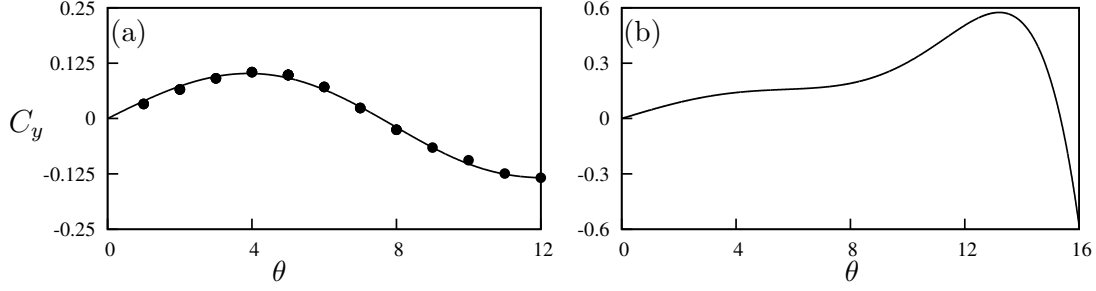


Figure 1.1: Lift coefficient,  $C_y$ , as a function of incidence angle  $\theta$ , for a static square cross section. (a) Data from simulations at  $Re = 200$  and (b) data from Parkinson and Smith (1964) at  $Re = 22300$ . The values at points ( $\bullet$ ) are acquired from direct numerical simulations. Curves in both plots are 7th-order interpolating polynomials used to interpolate the fluid forcing for the QSS model.

### 1.0.1 Static body results

The main data acquisition tool for galloping is the QSS model. As discussed in chapter , the QSS model uses an interpolation polynomial of the static body lift data as the driving force of the QSS equation. These static body data and the polynomial data are presented here. Figure 1.1 shows the plots of time averaged  $C_y$  data as a function of  $\theta$ , as well as the interpolation polynomial curves. Data are acquired for high and low Reynolds numbers. For high Reynolds numbers, the static body polynomial data are obtained from Parkinson and Smith (1964) while for low Reynolds numbers a 7<sup>th</sup> order non-linear least square regression fit on static body DNS simulations were used. The coefficients of these polynomials are presented in table 1.1.

There are several differences that can be observed between high and low Reynolds number data. The peak value of  $C_y$  is significantly lower at  $Re = 200$  ( $C_y = 0.12$  at  $5^\circ$ ) compared to  $Re = 22300$  ( $C_y = 0.57$  at  $13^\circ$ ). The inflection point present around  $8^\circ$  for  $Re = 22300$  is not present at  $Re = 200$ . This agrees with the findings of Luo et al. (2003). Luo et al. (2003) concluded that hysteresis in the system response occurs due to the inflection point in the  $C_y$  curve. Therefore, hysteresis could not be observed at  $Re = 200$ .

The range of incident flow angles where  $C_y$  remains positive is narrow at  $Re = 200$  ( $0^\circ < \theta \leq 7^\circ$ ) compared to  $Re = 22300$  ( $0^\circ < \theta \leq 15^\circ$ ). This positive range sustains galloping, as the power is only transferred from the fluid to the supporting structure within

Case	$a_1$	$a_3$	$a_5$	$a_7$
$Re = 200$	2.32	197.8	4301.7	30311.9
$Re = 22300$	2.69	168	1670	59900

Table 1.1: Coefficient values used in the 7th order interpolation polynomial for high ( $Re = 22300$ ) and low ( $Re = 200$ ) Reynolds numbers. These data are used as input data to calculate the right-hand side of Eq. ?? throughout this study.

this range of incident angles. This is because the fluid forces are acting in the direction of velocity of the body, or in phase with, the oscillating body as demonstrated by equation ???. Incident angles beyond this range suppress the galloping as power is transferred in the opposite direction, i.e; from body to fluid. Thus, it is expected that the transferred power at  $Re = 200$  to be significantly lower than at  $Re = 22300$ , because of the relative low values of  $C_y$  and the narrow range of positive  $C_y$  at  $Re = 200$ .

### 1.0.2 Formulation of the new dimensionless groups $\Pi_1$ and $\Pi_2$

The natural time scales of the system can be found by solving for the eigenvalues of the linearised equation of motion (Eq:??), namely

$$m\ddot{y} + c\dot{y} + ky = \frac{1}{2}\rho U^2 \mathcal{A}a_1 \left( \frac{\dot{y}}{U} \right), \quad (1.1)$$

which is a simplified version of the equation of motion presented in equation ?? with the polynomial series for the lift force truncated at the linear term.

Combining the  $\dot{y}$  terms and solving for eigenvalues gives

$$\lambda_{1,2} = -\frac{1}{2} \frac{c - \frac{1}{2}\rho U \mathcal{A}a_1}{m} \pm \frac{1}{2} \sqrt{\left[ \frac{c - \frac{1}{2}\rho U \mathcal{A}a_1}{m} \right]^2 - 4 \frac{k}{m}}. \quad (1.2)$$

If it is assumed that the spring is relatively weak,  $k \rightarrow 0$ , a single non-zero eigenvalue remains. This eigenvalue is

$$\lambda = -\frac{c - \frac{1}{2}\rho U \mathcal{A}a_1}{m}. \quad (1.3)$$

## 1. INTRODUCTION

---

Further, if it is assumed that the mechanical damping is significantly weaker than the fluid-dynamic forces on the body,  $c \rightarrow 0$  and

$$\lambda = \frac{\frac{1}{2}\rho U \mathcal{A} a_1}{m}. \quad (1.4)$$

In this form,  $\lambda$  represents the inverse time scale of the motion of the body due to the effect of the long-time fluid-dynamic forces. In fact, the terms can be regrouped and  $\lambda$  written as

$$\lambda = \frac{a_1}{m^*} \frac{U}{D} \quad (1.5)$$

Written this way, the important parameters that dictate this inverse time scale are clear. The rate of change in the fluid-dynamic force with respect to angle of attack when the body is at the equilibrium position,  $\partial C_y / \partial \alpha$ , is represented by  $a_1$ . The mass ratio is represented by  $m^*$ . The inverse advective time scale of the incoming flow is represented by the ratio  $U/D$ . Increasing  $a_1$  would mean the force on the body would increase more rapidly with small changes in the angle of attack,  $\theta$ , or transverse velocity. Equation 1.5 shows that such a change will increase the inverse time scale, or analogously decrease the response time of the body. Increasing the mass of the body, thereby increasing  $m^*$ , has the opposite effect. The inverse time scale is decreased, or as might be expected, a heavier body will respond more slowly.

This timescale can then be used to non-dimensionalize the equation of motion, and to find the relevant dimensionless groups of the problem. It was suggested by Shiels et al. (2001); Leonard and Roshko (2001) to use a flow-based timescale such  $D/U$  for the characteristic time for flow-induced vibration problems, rather than a structural-based timescale such as the natural frequency. This point is discussed further in ?. Here, this advective time is further scaled by the mass ratio  $m^*$ , as suggested from the eigenvalues of the linearized equation of motion. Hence, if the non-dimensional time,  $\tau$ , is defined such that  $\tau = t(a_1/m^*)(U/D)$ , the equation of motion presented in equation ?? can be non-dimensionalized as

$$\ddot{Y} + \frac{m^*}{a_1^2} \frac{k D^2}{m U^2} Y = \left( \frac{1}{2} - \frac{m^*}{a_1} \frac{c D}{m U} \right) \dot{Y} - \frac{a_1 a_3}{m^*{}^2} \dot{Y}^3 + \frac{a_1^3 a_5}{m^*{}^4} \dot{Y}^5 - \frac{a_1^5 a_7}{m^*{}^6} \dot{Y}^7. \quad (1.6)$$

The coefficients can be regrouped into combinations of non-dimensional groups, and



rewritten as

$$\ddot{Y} + \frac{4\pi^2 m^{*2}}{U^{*2} a_1^2} Y = \left( \frac{1}{2} - \frac{c^* m^*}{a_1} \right) \dot{Y} - \frac{a_1 a_3}{m^{*2}} \dot{Y}^3 + \frac{a_1^3 a_5}{m^{*4}} \dot{Y}^5 - \frac{a_1^5 a_7}{m^{*6}} \dot{Y}^7, \quad (1.7)$$

where  $U^*$  is the reduced velocity typically used as an independent variable in vortex-induced vibration studies and  $c^* = cD/mU$  is a non-dimensional damping parameter.

Equation 1.7 shows there are five non-dimensional parameters that play a role in setting the response of the system. These are the stiffness (represented by the reduced velocity  $U^*$ ), the damping  $c^*$ , the mass ratio  $m^*$ , and the geometry and  $Re$ , represented by the coefficients of the polynomial fit to the  $C_y$  curve,  $a_n$ . The grouping of these parameters into two groups in equation 1.7 which arise by non-dimensionalising using the natural time scale of the galloping system, suggests there are two groups besides geometry (represented by  $a_n$ ) and  $Re$  that dictate the response:  $\Gamma_1 = 4\pi^2 m^{*2}/U^{*2} a_1^2$  and  $\Gamma_2 = c^* m^*/a_1$ . For a given geometry and Reynolds number,  $\Gamma_1$  can be thought of as a combined mass-stiffness, whereas  $\Gamma_2$  can be thought of a combined mass-damping parameter. It is assumed that during galloping the stiffness plays only a minor role because, galloping time periods are significantly large which implies that  $k \rightarrow 0$ . Therefore,  $\Gamma_2$  seems a likely parameter to collapse the data. In fact, in the classic paper on galloping from Parkinson and Smith (1964), galloping data from wind tunnel tests is presented in terms of a parameter that can be shown to be the same as  $\Gamma_2$ .

All of the quantities that make up  $\Gamma_1$  and  $\Gamma_2$  can, in theory, be known before an experiment is conducted. However, the quantity  $a_1$  is a relatively difficult one to determine, requiring static body experiments or simulations. Here, the geometry is unchanged and results are only being compared at the same  $Re$ . Hence, suitable parameters can be formed by multiplying  $\Gamma_1$  and  $\Gamma_2$  by  $a_1^2$  and  $a_1$  respectively, to arrive at a mass-stiffness parameter  $\Pi_1 = 4\pi^2 m^{*2}/U^{*2}$ , and a mass-damping parameter defined as  $\Pi_2 = c^* m^*$ .

Equation 1.7 can be re-written explicitly in terms of  $\Pi_1$  and  $\Pi_2$  to give

$$\ddot{Y} + \Pi_1 Y = \Pi_2 \dot{Y} - \frac{a_1 a_3}{m^{*2}} \dot{Y}^3 + \frac{a_1^3 a_5}{m^{*4}} \dot{Y}^5 - \frac{a_1^5 a_7}{m^{*6}} \dot{Y}^7. \quad (1.8)$$


---

### 1.0.3 Comparison of $\Pi_1$ and $\Pi_2$ with classical VIV parameters

Figure 1.2 shows the comparison of mean power data at  $Re = 200$  presented using different independent variables. Subfigures (a), (c) and (e) show the displacement amplitude, velocity amplitude and the mean power as a function of the classic VIV parameter,  $U^*$  for various damping ratios  $\zeta$ . Subfigures (b), (d) and (f) shows the same data as a function of  $\Pi_2$ , for various, reasonably high values of  $\Pi_1$ , as defined above in section 1.0.2. The data presented using the classical VIV parameters follows the same trends as Barrero-Gil et al. (2010). Barrero-Gil et al. (2010) and Vicente-Ludlam et al. (2014) observed that the maximum dimensionless power is achieved at two times the velocity at which the galloping starts. A similar conclusion can be drawn from the data presented here in figures 1.2. However, the data presented using the dimensionless group formulated using the natural time scales of the system shows an excellent collapse for both velocity amplitude and mean power, showing that the power is essentially dictated by  $\Pi_2$ . This implies that unlike VIV which is a type of resonant phenomenon, the natural frequency of the system which is used to scale  $U^*$ ,  $\zeta$  and  $\Pi_1$  does not have a large influence on the system behaviour in these cases.

### 1.0.4 Comparison of power between high and low $Re$ data

The marked success of the collapse using  $\Pi_2$  for the  $Re = 200$  case, particularly of the mean power, could also be replicated for the higher  $Re$  case at  $Re = 22300$ . Figure 1.3 presents the mean power for high  $Re$  cases for selected values of  $\Pi_1$ . It is shown that the data collapse in both cases, demonstrating the validity of using  $\Pi_2$  as an independent variable.

Hysteresis could be observed for the  $Re = 22300$  case. The different solutions could be obtained by manipulating the initial conditions (initial displacement) of the system. The upper branch was obtained by giving an initial displacement which was higher than the expected amplitude while the lower branch was obtained by providing a lower initial displacement than the expected amplitude. Although theory shows a possible third state, it is an unstable branch which could not be achieved with a time integration method such as that employed in this study. This was also observed by Vio et al. (2007).

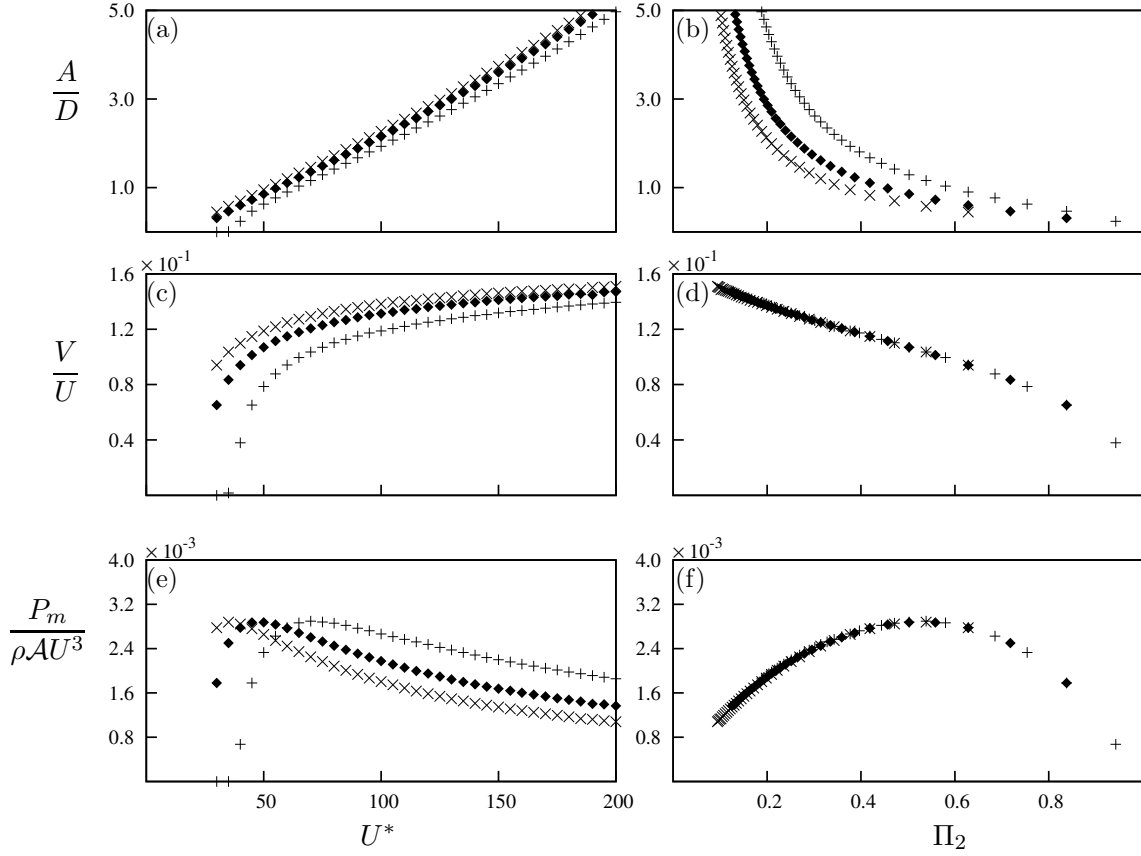


Figure 1.2: Displacement amplitude, velocity amplitude and dimensionless mean power data as functions of two different independent variables. Data presented in (a), (c) and (e) using the classical VIV parameter  $U^*$ , obtained at  $Re = 200$  and  $m^* = 20$  at three different damping ratios:  $\zeta = 0.075$  ( $\times$ ),  $\zeta = 0.1$  ( $\blacklozenge$ ) and  $\zeta = 0.15$  (+). (b) (d) and (f) are the same data presented using the combined mass-damping parameter ( $\Pi_2$ ) as the independent variable. Even though  $\Pi_1$  varies in the range of  $0.4 \leq \Pi_1 \leq 17.5$ , it is clear that the power is a function of  $\Pi_2$  only.

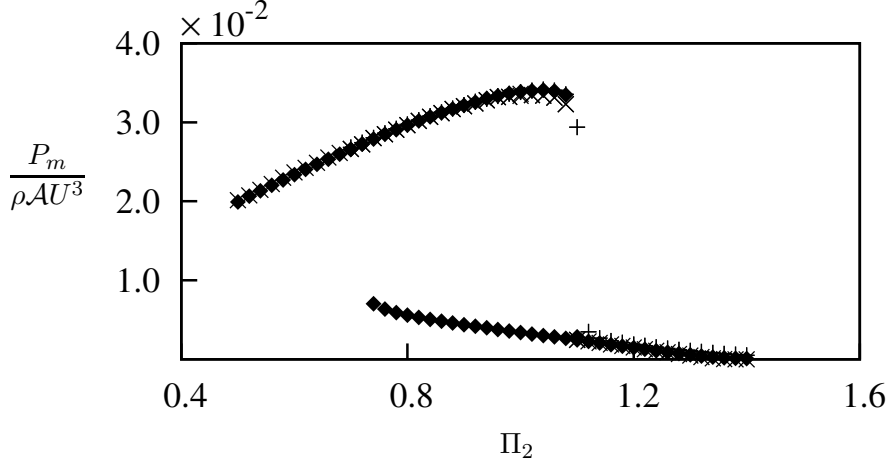


Figure 1.3: Dimensionless mean power as a function of  $\Pi_2$ . Data presented at  $Re = 22300$ ,  $\Pi_1 = 200$  ( $\times$ ),  $\Pi_1 = 2000$  ( $\blacklozenge$ ) and  $\Pi_1 = 10000$  ( $+$ ). Hysteresis could be observed at high  $Re$ .

### 1.0.5 Dependence on mass-stiffness, $\Pi_1$

The results of sections 1.0.3 and 1.0.4 show that the mean extracted power is essentially a function of a single variable, the combined mass-damping  $\Pi_2$ . However, the timescale analysis of section 1.0.2 showed that a second variable, the combined mass-stiffness  $\Pi_1$  should also play a role. Previous studies (see, for example Bouclin (1977)) have also indicated a complex interaction between the amplitude and natural frequency, particularly for high natural frequencies (or equivalently, low values of  $\Pi_1$ ). Here, the impact of  $\Pi_1$  is investigated further. Overall, the system behaviour can be separated into two wide regimes; that for “high”  $\Pi_1$  and that for “low”  $\Pi_1$ . These two regimes are further investigated and explained in this following section.

Figure 1.4 shows the mean power as a function of  $\Pi_2$  for a range of values of  $\Pi_1$ . Two subfigures are shown; subfigure (a) shows data for  $\Pi_1 \geq 10$ , while (b) shows data for  $\Pi_1 \leq 10$ . In figure 1.4(a), the collapse of the mean power is excellent, showing that for  $\Pi_1 \geq 10$ , the mean power is independent of  $\Pi_1$ .

For low values of  $\Pi_1 \leq 10$ , figure 1.4(b) shows that the predicted mean power increases as  $\Pi_1$  is decreased, indicating that the mean power is a weak function of  $\Pi_1$  at low  $\Pi_1$  levels. This provides the distinction between high and low  $\Pi_1$  regimes. For high values where  $\Pi_1 \geq 10$ , the mean extracted power is a function of  $\Pi_2$  only; for low values where

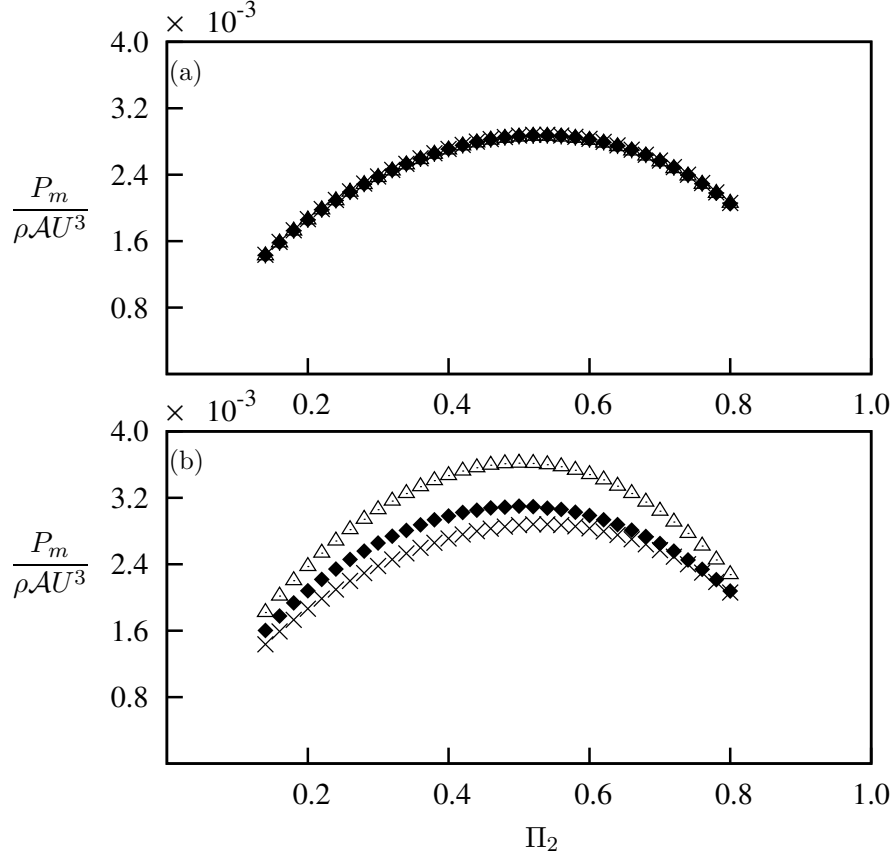


Figure 1.4: Dimensionless mean power as a function of  $\Pi_2$  obtained using the QSS model at  $Re = 200$ . (a) High  $\Pi_1$ ; data presented at four different combined mass-stiffness levels.  $\Pi_1 = 10$  ( $m^* = 20$ ,  $U^* = 40$ ) ( $\times$ ),  $\Pi_1 = 100$  ( $m^* = 80$ ,  $U^* = 50$ ) ( $+$ ),  $\Pi_1 = 500$  ( $m^* = 220$ ,  $U^* = 60$ ) ( $\blacklozenge$ ) and  $\Pi_1 = 1000$  ( $m^* = 400$ ,  $U^* = 40$ ) ( $\triangle$ ). (b) Low  $\Pi_1$ ; data presented at  $\Pi_1 = 10$  ( $\times$ ),  $\Pi_1 = 0.1$  ( $\blacklozenge$ ), and  $\Pi_1 = 0.01$  ( $\triangle$ ).

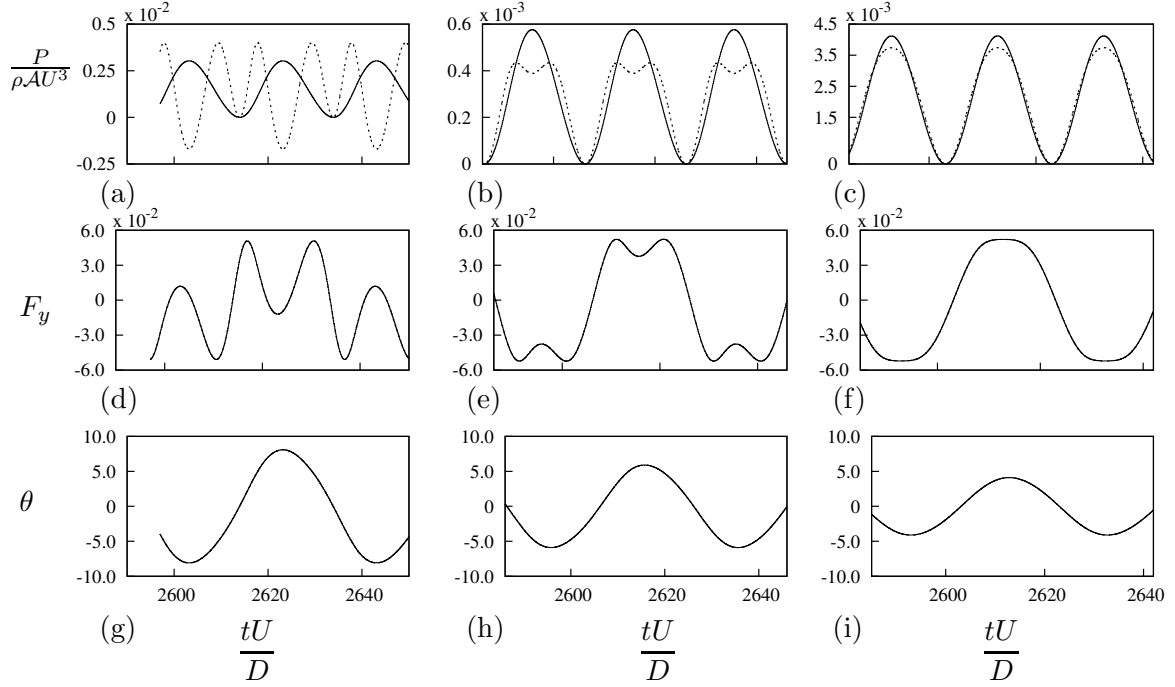


Figure 1.5: Time histories of  $P_t$ ,  $P_d$ ,  $F_y$  and  $\theta$  at  $\Pi_2 = 0.15, 0.54$  and  $0.8$  from the QSS model. Data was obtained at  $m^* = 20$ ,  $\Pi_1 = 10$  and  $Re=200$ . The time histories of  $P_d$  (—) and  $P_t$  (---) are presented for: (a)  $\Pi_2 = 0.15$ ; (b)  $\Pi_2 = 0.54$ ; (c)  $\Pi_2 = 0.8$ . Time histories of the instantaneous force  $F_y$  for: (d)  $\Pi_2 = 0.15$ ; (e)  $\Pi_2 = 0.54$ ; (f)  $\Pi_2 = 0.8$ . Time histories of the instantaneous angle  $\theta$  for: (g)  $\Pi_2 = 0.15$ ; (h)  $\Pi_2 = 0.55$ ; (i)  $\Pi_2 = 0.8$ .

$\Pi_1 < 10$ , the mean extracted power is a weak function of  $\Pi_1$ .

Regardless of the value of  $\Pi_1$ , the variation of the mean extracted power with  $\Pi_2$  is essentially the same. With increasing  $\Pi_2$ , the mean extracted power initially increases, before reaching some maximum value and then decreasing. This relationship between power and  $\Pi_2$  can be explained by analysing the time histories of selected cases. Data at  $\Pi_1 = 10$ ,  $m^* = 20$  and  $Re = 200$  are shown in figure 1.5 and are analysed as an example. Values of  $\Pi_2$  less than (region 1), equal to (region 2), and greater than (region 3) the value where the mean extracted power is a maximum are analysed as examples.

The instantaneous power from the fluid to the body can be expressed as  $P_t = F_y \dot{y}$ . Similarly the dissipated power due to the mechanical damping can be expressed as  $P_d = (c\dot{y})\dot{y}$ . The time average of these two quantities, described in equations ?? and ?? must be equal due to energy conservation.

At region 1 ( $\Pi_2 = 0.15$ ) the damping is low in comparison with region 2 and 3. While this may lead to larger oscillations, damping is required to dissipate and therefore extract power according to equation ???. Therefore, the low damping in this region leads to a low mean power output. Fig.1.5 (a) shows that  $P_d$  (the power dissipated by damping) becomes negative over some portion of the cycle. This is caused by the high velocity amplitude leading to the equivalent incident angle  $\theta$  to exceed the range where  $C_y$  is positive (i.e.  $0 < \theta < 6^\circ$  as shown in figure??(a)). In this portion of the cycle the fluid-dynamic force actually opposes the direction of travel and power is transferred from the structure to the fluid during those times. From an energy perspective, the mechanical damping is not sufficient to remove the energy transferred from the fluid to the structure through work during other times of the cycle because  $\Pi_2$  is substantially low. Therefore this excess energy is transferred back to the fluid as depicted by the negative region of  $P_d$ .

At region 3 where  $\Pi_2 = 0.8$  the damping constant is high and a clear sinusoidal signal is observed for both  $P_d$  and  $P_t$  in figure 1.5(c). Figures 1.5(f) and 1.5(i) show that equivalent incident angle  $\theta$  (which for small values, is proportional to the transverse velocity of the body) is in phase with  $F_y$ . The velocity amplitude in this case is small and  $\theta$  is within the range where the fluid-dynamic force increases with the incident angle (i.e.  $0 < \theta \leq 5^\circ$  as shown in figure 1.1(a)). According to equation ??, these conditions are suitable for high power output. However in this case, the high damping limits the velocity amplitude and results in relatively low fluid dynamic forces.

At region 2 ( $\Pi_2 = 0.54$ ), a balance is found between high and low values of damping.  $P_d$  is not a pure sinusoidal signal, however the signal remains periodic. From the time history graph of  $P_d$ , two ‘peaks’ are present in a single half cycle as shown in figure 1.5(b). In this case, the velocity amplitude actually exceeds the equivalent incident angle where the fluid-dynamic forces peaks (i.e.  $\theta = 5^\circ$  in ?? (a)). The dips in  $P_d$  between the two peaks approximately correspond to the time where the transverse velocity is higher than 0.09 and  $F_y$  is decreasing with increasing transverse velocity. The mean power output is at its maximum. This is due to the fact that this region is the best compromise between region 1 and 3. The damping is high enough to obtain a high power output while not so high that the motion is completely suppressed.

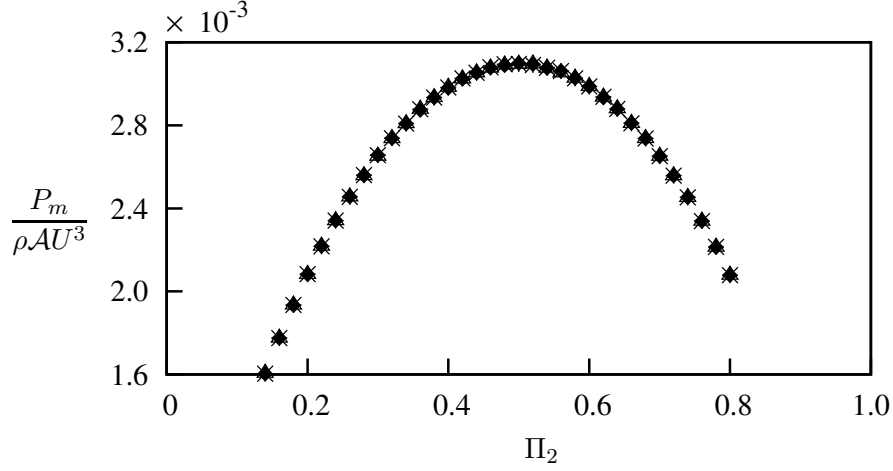


Figure 1.6: Dimensionless mean power as a function of  $\Pi_2$  obtained using QSS model at  $\Pi_1 = 0.1$ . Data presented at  $m^* = 2$  ( $\blacklozenge$ ),  $m^* = 20$  ( $\triangle$ ) and  $m^* = 50$  ( $*$ ). The mass ratio does not have an effect on  $\Pi_1$  even at low  $\Pi_1$ .

#### 1.0.6 Dependence on the mass ratio $m^*$

While for high values of  $\Pi_1$  it is clear that the mean extracted power is a function of  $\Pi_2$  only, a question arises for low values of  $\Pi_1$ ; is the variation in the mean extracted power purely a function of  $\Pi_1$ , or is it also a function of the mass ratio  $m^*$ ? To answer this question, the model has been solved for a fixed value of  $\Pi_1$ , but for varying values of  $m^*$ . This means that  $\Pi_1$  was varied by changing the system stiffness.

Figure 1.6 shows the mean extracted power as a function of  $\Pi_2$ , for a fixed  $\Pi_1 = 0.1$ , for three different values of  $m^*$ . From the figure it is clear that the results are independent of  $m^*$ , and are a function of  $\Pi_1$  and  $\Pi_2$  only.



# BIBLIOGRAPHY

---

- Barrero-Gil, A., Alonso, G., Sanz-Andres, A., Jul. 2010. Energy harvesting from transverse galloping. *Journal of Sound and Vibration* 329 (14), 2873–2883.
- Barrero-Gil, A., Sanz-Andrés, A., Roura, M., Oct. 2009. Transverse galloping at low Reynolds numbers. *Journal of Fluids and Structures* 25 (7), 1236–1242.
- Bernitsas, M. M., Ben-Simon, Y., Raghavan, K., Garcia, E. M. H., 2009. The VIVACE Converter: Model Tests at High Damping and Reynolds Number Around  $10^5$ . *Journal of Offshore Mechanics and Arctic Engineering* 131 (1), 011102.
- Bernitsas, M. M., Raghavan, K., Ben-Simon, Y., Garcia, E. M. H., 2008. VIVACE (Vortex Induced Vibration Aquatic Clean Energy): A new concept in generation of clean and renewable energy from fluid flow. *Journal of Offshore Mechanics and Arctic Engineering* 130 (4), 041101–15.
- Bouclin, D. N., 1977. Hydroelastic oscillations of square cylinders. Master’s thesis, University of British Columbia.
- Lee, J., Bernitsas, M., Nov. 2011. High-damping, high-Reynolds VIV tests for energy harnessing using the VIVACE converter. *Ocean Engineering* 38 (16), 1697–1712.
- Leonard, A., Roshko, A., 2001. Aspects of flow-induced vibrations. *Journal of Fluids and Structures* 15, 415–425.
- Luo, S., Chew, Y., Ng, Y., Aug. 2003. Hysteresis phenomenon in the galloping oscillation of a square cylinder. *Journal of Fluids and Structures* 18 (1), 103–118.
- Parkinson, G. V., Smith, J. D., 1964. The square prism as an aeroelastic non-linear oscillator. *The Quarterly Journal of Mechanics and Applied Mathematics* 17 (2), 225–239.

## BIBLIOGRAPHY

---

- Raghavan, K., Bernitsas, M., Apr. 2011. Experimental investigation of Reynolds number effect on vortex induced vibration of rigid circular cylinder on elastic supports. *Ocean Engineering* 38 (5-6), 719–731.
- Shiels, D., Leonard, A., Roshko, A., 2001. Flow-induced vibration of a circular cylinder at limiting structural parameters. *Journal of Fluids and Structures* 15, 3–21.
- Vicente-Ludlam, D., Barrero-Gil, A., Velazquez, A., 2014. Optimal electromagnetic energy extraction from transverse galloping. *Journal of Fluids and Structures* 51, 281–291.
- Vio, G., Dimitriadis, G., Cooper, J., Oct. 2007. Bifurcation analysis and limit cycle oscillation amplitude prediction methods applied to the aeroelastic galloping problem. *Journal of Fluids and Structures* 23 (7), 983–1011.